Int J Fract (2020) 221:171–190
https://doi.org/10.1007/s10704-020-00421-x

ORIGINAL PAPER

A computationally efficient approach for predicting toughness enhancement in ceramic composites with tailored inclusion arrangements

Aditya R. Thakur · Congjie Wei · Chenglin Wu · Jeremy L. Watts · Charles S. Wojnar

Received: 22 March 2019 / Accepted: 7 January 2020 / Published online: 18 January 2020

Abstract Advanced manufacturing techniques such as extrusion-based methods have enabled the fabrication of ceramic composites with ordered inclusion phases (i.e. the size and position of the inclusion can be precisely controlled) to improve their overall strength and toughness. Conventional theories, simulation approaches, and experimental methods for analyzing fracture in composites with randomly dispersed inclusion phases (resulting in homogeneous, isotropic effective properties) become inadequate at understanding and designing composites with ordered inclusions for enhancing effective properties such as toughness. In addition, existing methods for analyzing fracture in composites can be computationally expensive and pose challenges in accurately capturing experimentally observed fracture growth. For example, extended finite element and phase-field methods are computationally expensive in evaluating the large design space of possible inclusion arrangements enabled by the new manufacturing techniques. In this work, a closed-form analytical model for the mixed-mode stress intensity factor in a composite with selected inclusion arrangements is presented, which expedites the analysis for various composite designs. Moreover, the fracture initiation calculation is adapted to approximate crack propagation with computational efficiency. The accuracy of this model for predicting fracture initiation is validated by linear elastic fracture mechanics analysis using the finite element method. The prediction of fracture propagation is validated using a phase-field model, as well as a 4-point bending experiment. Finally, the model is applied to analyze three different composite inclusion arrangements to study the effect of various material combinations and geometries on the overall toughness of the composite; a complete sampling of (and optimization) over the entire design space, however, is beyond the scope of this work. The relative increase in crack length (compared to a homogeneous material) is used as a metric to compare the relative toughness of three different composite designs. Within these designs, using the fast-running approximate method, the effect of the ratio of inclusion radius to inclusion spacing, and the elastic mismatch on the resulting crack length are compared to determine the composite arrangements that result in the greatest toughness

A. R. Thakur
Department of Mechanical and Aerospace Engineering, Missouri University of Science and Technology, 400 W. 13th St., Rolla, MO 65409, USA

C. Wei · C. Wu (✉)
Department of Civil, Architectural, and Environmental Engineering, Missouri University of Science and Technology, 1401 N. Pine St., Rolla, MO 65409, USA
e-mail: wuch@mst.edu

J. L. Watts
Department of Materials Science and Engineering, Missouri University of Science and Technology, 1400 N. Bishop, Rolla, MO 65409, USA

C. S. Wojnar
Computational Engineering Division, Lawrence Livermore National Laboratory, 7000 East Ave., Livermore, CA 94550, USA

enhancement for selected material properties. In particular, a multi-phase cubic array resulted in the greatest toughness enhancement of the designs considered.

Keywords Patterned inclusion · Fracture · Ceramic composite · Analytical approximation

1 Introduction

Ceramic materials exhibit many useful properties such as high strength, stiffness, melting temperatures, and chemical stability. However, the fundamental problem preventing their widespread use in structural applications is their low fracture toughness. The brittle nature of ceramics renders such structures susceptible to complex crack paths. Thus, the failure of ceramic structures is difficult to predict. As a result, the safety of ceramic structures is often given by probability distribution functions (Danzer 1992; Evans and Wiederhorn 1984). Uncertainty in the failure strength of such structures requires large safety factors that increase cost, require more material, and increase weight. Due to these issues, a longstanding goal has been to find ways of increasing the toughness of ceramics.

One approach to increase toughness, which is often found in nature, is to create ceramic composites and hierarchical structures (Gao et al. 2003; Ritchie et al. 2009). This approach has been explored in experiments (D'Angio' et al. 2018) and theoretical analysis (Faber and Evans 1983a, b; Miller et al. 1998) to determine how inclusion phases at different scales affect overall strength and toughness. The introduction of secondary phases and hierarchy leads to toughening mechanisms such as crack deflection, interface debonding, and fracture branching.

Currently, particulate ceramic composites are generally manufactured using the process of powder sintering where secondary phase particles are mixed with the matrix material. After sintering, the secondary particles form a random distribution of inclusions. One limitation of this process is that the precise arrangement of the inclusions, which affects crack propagation, cannot be controlled. To overcome this limitation, co-extrusion techniques have been developed that enable the position and geometry of inclusions to be tailored (Hoy et al. 1998). This method will be adapted to create ceramic composites with precisely positioned cylindrical inclusions with specified radii. With the ability to carefully control composite geometry parameters (such as inclusion spacing and the periodic pattern) enabled by this manufacturing technique, a wide range of composites can be created that result in different fracture behavior. However, with the large design space, an efficient and sufficiently accurate method is necessary to feasibly search for optimal composite arrangements.

To analyze fracture initiation and propagation in different composite arrangements, we developed an analytical model for the mixed-mode stress intensity factor of a kinked crack within a multi-phase composite with multiple inclusions, which was validated with experiments and was compared with linear elastic fracture mechanics (for initiation) and phase-field simulations (for propagation). Our approach combines the previous analytical models for the mode I (Li and Chen 2002) and mode II (Yang et al. 2004) stress intensity factors of a straight crack near an inclusion and a model for the local mode I and II stress intensity factors of a kinked crack tip under far-field mode I and II loading (He and Hutchinson 1989). Using this model and an incremental crack extension method (described later), the toughness of several different composite arrangements was computed based on a crack length metric.

2 Mixed mode stress intensity factor of a kinked crack near inclusions

In the following, we analyze the mixed-mode stress intensity factor at a kinked crack tip in the vicinity of two nearby inclusions as shown in Fig. 1. The approach is general and can be applied to different composite arrangements with more than two inclusions (as will be shown later), but as a starting example, we restrict to the geometry in Fig. 1. In particular, the change in stress field due to inclusions decays to the far-field stress away from the inclusions. It is therefore a reasonable assumption that only the two nearest inclusions (in a possible array of inclusions) will significantly affect the crack. As will be seen in subsequent sections, experiments will be performed on notched specimens in a 4-point bending configuration. In our analysis, we zoom in on the crack tip in the specimen assuming a far-field loading is applied (due to 4-point bending), which results in a mode I and II stress intensity factor in a homogeneous material with a straight crack, K_1 and K_2, respectively. We now assume there is a kinked crack with length,

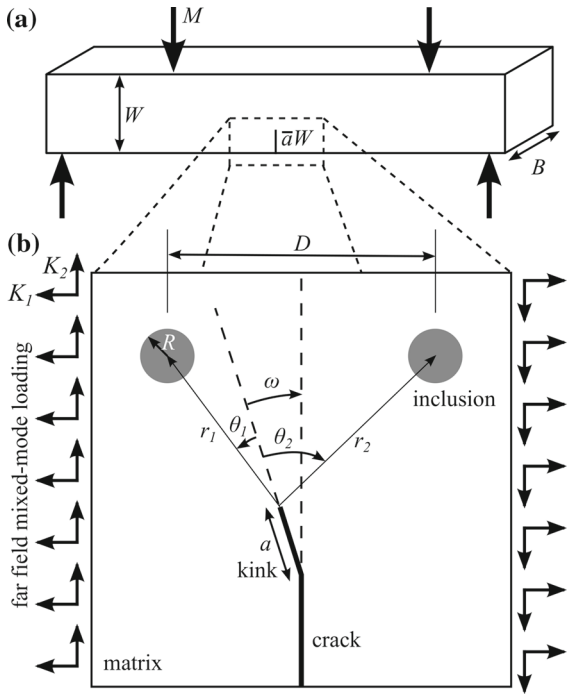

Fig. 1 Illustration of **a** the 4-point bending geometry and **b** the geometry of a kinked crack between two inclusions in a specimen subjected to far field mixed loading (zoomed in region near the notch in the 4-point bending specimen)

a, at an angle, ω, relative to the initial straight crack. The radius and angle from the center of the two circular inclusions (relative to the tip of the kinked crack segment) are (r_1, θ_1) and (r_2, θ_2), respectively. The radius of the inclusions (assumed equal) is R and their separation distance is D as shown in Fig. 1b.

2.1 Mode I stress intensity factor on a straight crack in a 4-point bending test

As a first step, we assume a moment, M, is applied to the 4-point bending specimen. To analyze the influence of the inclusions on the stress intensity factor, we first compute the stress intensity factor at the notch in the specimen due to the applied moment (assuming at this point the specimen is homogeneous without inclusions). For a 4-point bending experiment with a single edge notched specimen, the stress intensity factors (in mode I and mode II) due to the applied global loading on a straight crack without a kink is given by Anderson (2005),

$$K_1 = \frac{6M}{B\,W^{3/2}} \frac{\sqrt{2\tan\left(\frac{\pi\bar{a}}{2}\right)}}{\cos\left(\frac{\pi\bar{a}}{2}\right)} \times \left(0.923 + 0.199\left(1 - \sin\left(\frac{\pi\bar{a}}{2}\right)\right)^4\right), \quad K_2 = 0, \tag{1}$$

where B is the depth of the specimen, W is the width of the specimen, and $\bar{a} = a/W$ is the ratio of the notch length to the width of the specimen as shown in Fig. 1a.

2.2 Approximate stress intensity factor of a kinked crack

Next, the stress intensity factor of a kinked crack tip (added to the initial straight notch crack) is determined in order to mimic material defects at the crack tip. Due to the presence of nearby inclusions, the crack will prefer to propagate in a certain direction, which is initiated by small-scale defects that we approximate as an infinitesimal kink. The mode I and II stress intensity factors at a kinked crack in a linear elastic, isotropic, homogeneous material are, respectively, of the form (He and Hutchinson 1989)

$$K_I = \mathrm{Re}[c + d]K_1, \quad K_{II} = \mathrm{Im}[c - d]K_1, \tag{2}$$

where K_1 is the mode-I stress intensity factors due to the applied global loading on a straight crack without a kink given in (1), which is in turn related to the applied moment to the specimen. The parameters c and d are functions of the kink angle, ω, for an infinitesimal kink length (see Appendix 1). Note that we have proceeded by assuming an initial straight crack and setting $K_2 = 0$ in the result of He and Hutchinson (1989) to obtain (2).

2.3 Influence of a nearby inclusion on a straight crack

We now consider the influence of the inclusions on the stress intensity factors (mode I and II) of the kinked crack. Here we follow the analysis of Li and Chen (2002) and Yang et al. (2004) who derived an approximate form for the change in the mode I and II stress intensity factors, respectively, around a straight crack due to the presence of a nearby inclusion. Their approach is based on the influence of a perturbation in material properties on the stress intensity factor of a

straight crack (Lambropoulos 1986). For circular inclusions, the changes in stress intensity factor in mode I and II (for the $i = 1, 2$ inclusion) are, respectively,

$$\begin{aligned}\Delta K_{Ii} &= K_I \left(\frac{R}{r_i}\right)^2 \left(C_1 \cos\left(\frac{\theta_i}{2}\right) \cos\left(\frac{3\theta_i}{2}\right) \right. \\ &\quad \left. + C_2 (\sin\theta_i)^2 \cos\theta_i \right), \\ \Delta K_{IIi} &= K_{II} \left(\frac{R}{r_i}\right)^2 \left(C_3 \cos\theta_i + C_4 \cos(2\theta_i) \right. \\ &\quad \left. + C_5 \cos(3\theta_i) \right),\end{aligned} \tag{3}$$

where R is the (equal) radius of the inclusions, r_i is the distance of the ith inclusion from the crack tip, θ_i is the angle of the ith inclusion relative to the crack (cf. Fig. 1). Note that the integral results in Li and Chen (2002) and Yang et al. (2004) have been simplified by assuming the inclusion radius R is small compared to the distance between the inclusion and crack tip, r_i, to obtain (3); the original integral expression is computed by evaluating the integrand at the center of the inclusion and multiplying it by the inclusion area. It should also be noted that here we assume the kink length, while small compared to the initial crack, may not be small compared to the distance to the inclusions. Hence, the radius to the inclusions, r_i, is taken relative to the tip of the kinked crack (not the tip of the initial straight crack). Likewise, the angles of the inclusions are taken relative to the axis of the kinked portion of the crack as shown in Fig. 1b. The coefficients C_1, C_2, C_3, and C_4 are defined based on material properties (included in Appendix 1).

Once the change in stress intensity factor (for mode I and II) due to the ith inclusion is determined, ΔK_{Ii} and ΔK_{IIi}, the total stress intensity factor at the crack tip is found by adding to the stress intensity factor of the straight crack in a homogeneous material,

$$\begin{aligned}K_{I,\text{total}} &= K_I + \sum_{i=1}^{n} \Delta K_{Ii}, \\ K_{II,\text{total}} &= K_{II} + \sum_{i=1}^{n} \Delta K_{IIi},\end{aligned} \tag{4}$$

where n is the number of inclusions. Only two inclusions are shown in Fig. 1b ($n = 2$), but more can be included as necessary.

Finally, to establish a criterion for crack propagation, the energy release rate for the composite system is defined as (assuming the crack is inside the matrix)

$$J = \frac{\left(K_{I,\text{total}}\right)^2}{E_{\text{mat}}} + \frac{\left(K_{II,\text{total}}\right)^2}{\mu_{\text{mat}}}, \tag{5}$$

where μ_{mat} is shear modulus of matrix material. That is, the crack will tend to propagate in the direction of a kink angle corresponding to the maximum value of J.

2.4 Combined effect of crack kinking and nearby inclusions

The total mode I and mode II stress intensity factors $K_{I,\text{total}}$ and $K_{II,\text{total}}$, are computed via (4), where the stress intensity factors for the kinked crack (without inclusions), K_I and K_{II}, are computed via (2). To relate quantities to the experiment, the far field mode I stress intensity factor, K_1, used to compute the kinked crack stress intensity factors is computed using (1) as a function of the moment, M, applied to the 4-point bending specimen. Using these relations, the total stress intensity factor at a kinked crack in the vicinity of inclusions can be computed from the load in the 4-point bending test, inclusion properties, inclusion geometry, and inclusion arrangement.

At this point, the important assumptions in our analysis are highlighted: (i) the effect of kinking on the stress intensity factor assumes the kink length is infinitesimally small relative to the overall specimen (but not relative to the inclusion separation distance), (ii) the inclusions were circular with radii much smaller than their distance to the crack, and (iii) the analysis was simplified by assuming one-way coupling between the inclusions and the K-field. That is, the K-field around a crack was used to compute the stress inside the inclusions, which in turn, via the solution by Eshelby (1975), was used to compute the change in stress at the crack tip (and subsequently the change in stress intensity factor). In reality, the change in stress intensity factor would again influence the stress in the inclusion. This effect is neglected for simplicity. (iv) The matrix and inclusion materials are assumed to have the same Poisson ratio and comparable coefficients of thermal expansion to simplify the equations. This assumption yields reasonably accurate results compared to numerical results for the material system under consideration. Finally, (v) while the kinked crack length is assumed to be infinitesimally small, we treat the kinked portion of the crack as a straight crack when applying Eq. (3), which would

be slightly different than non-straight cracks induced by defects in the specimen.

2.5 Finite element validation for fracture initiation

In the following, the accuracy of the proposed analytical model for the mixed-mode stress intensity factor of a kinked crack in the presence of inclusions was examined through a case study using linear elastic fracture mechanics (LEFM) finite element analysis. The stress intensity factor and J-integral predictions were extracted from the finite element analysis.

The mode I and mode II stress intensity factors and J-integral from (4) and (5) were compared to the result from LEFM obtained via finite element analysis using Abaqus. When simulating dual-phase composites using finite element analysis, the interaction between the crack and the inclusions is generally predicted more accurately through a 3-dimensional model. However, finite element analysis produces similar stress maxima for 2-dimensional plane strain as well as 3-dimensional analyses in comparison to plane stress as the cracks are believed to mostly originate at the core of the specimen (Twickler et al. 1986). A 2-dimensional plane strain model (using shell elements) with circular inclusions was thus preferred over a 3-dimensional model to simplify the analyses (Fett et al. 1996; Helsing 1999; Lipetzky and Knesl 1995; Sih et al. 1970; Stam et al. 1994; Wang et al. 1998). The elements were 4-node bilinear plane strain quadrilaterals with reduced integration scheme.

A representative sample geometry of the 4-point bending test with a 1 mm long centered notch and 0.2 mm kink was selected (see Fig. 2a). The two-phases of material in the specimen were represented using a partition function. A ramped displacement of 0.1 mm was applied via two contact points on the top, and the resulting stress and strain field was computed. A dense mesh with a smallest element size of 4 μm was generated and a square-root singularity was defined near the crack-tip (see Fig. 2b). Note that the mesh shown in Fig. 2c was used in the phase-field simulation discussed in a later section. The material properties are shown in Table 1. Note that the Poisson ratios for the two materials in Table 1 are not identical. Nonetheless, the values are similar such that selecting $\nu = 0.16$ in the finite element simulation (in order to compare with the analytical model) resulted in an accurate approximation.

The distance between the inclusions, D, and the radius of the inclusions, R, were varied to characterize the accuracy of the analytical model by comparing the stress intensity factors and J-integral predicted by the analytical model and finite element solution. The two different inclusion radii examined were 300 μm and 500 μm. These two radii were considered for the simulation based on their practicality to be fabricated using the co-sintering manufacturing process. This is because exceedingly large inclusions lead to undesirable microcracks at the interface, while extremely small inclusions will result in negligible changes in the fracture behavior. The distances between the inclusions were varied from 1.5 to 2 mm. It was observed that the influence of the inclusions diminished as the distance between them was increased. Thus, the maximum separation distance was limited to 2 mm as increasing the distance resulted in little change in the stress intensity factor. A contour integral (for evaluating the J-integral) that encircled the crack tip but that did not intersect the inclusions was introduced into the simulation.

For each geometric combination of inclusion radius and separation distance, the mode I and mode II stress intensity factors (see (4)) and the J-integral (see (5)) were plotted versus the kink angle at the end of the notch from 0° to 90° as shown in Fig. 3 (negative angles were not considered here due to symmetry). The markers represent the finite element prediction and the solid lines correspond to the analytical solution. Figure 3a–c, plot the relative stress intensity factors in model I and II, and the relative J-integral, respectively, versus kink angle for different inclusion separation distances, D, and fixed radius, R. The relative K_I and J were normalized by their value at zero kink angle $\omega = 0$. The relative K_{II} was normalized by its maximum value in the homogeneous specimen. Figure 3c–e, also show the same plots, but now with different radii, R, but fixed separation distance, D.

The analytical model accurately captures the variation of the stress intensity factors and J-integral in the range of kink angles considered (up to 90°). As postulated through the small kink angle assumption, the accuracy of the analytical model is higher for smaller kink angles. Moreover, at larger kink angles, the analytical model is less accurate for the cases with inclusions than the one without inclusions (owing to the assumptions made when incorporating inclusions in the model). To summarize, for this specimen geometry, the analytical model predictions are within 5% (at most)

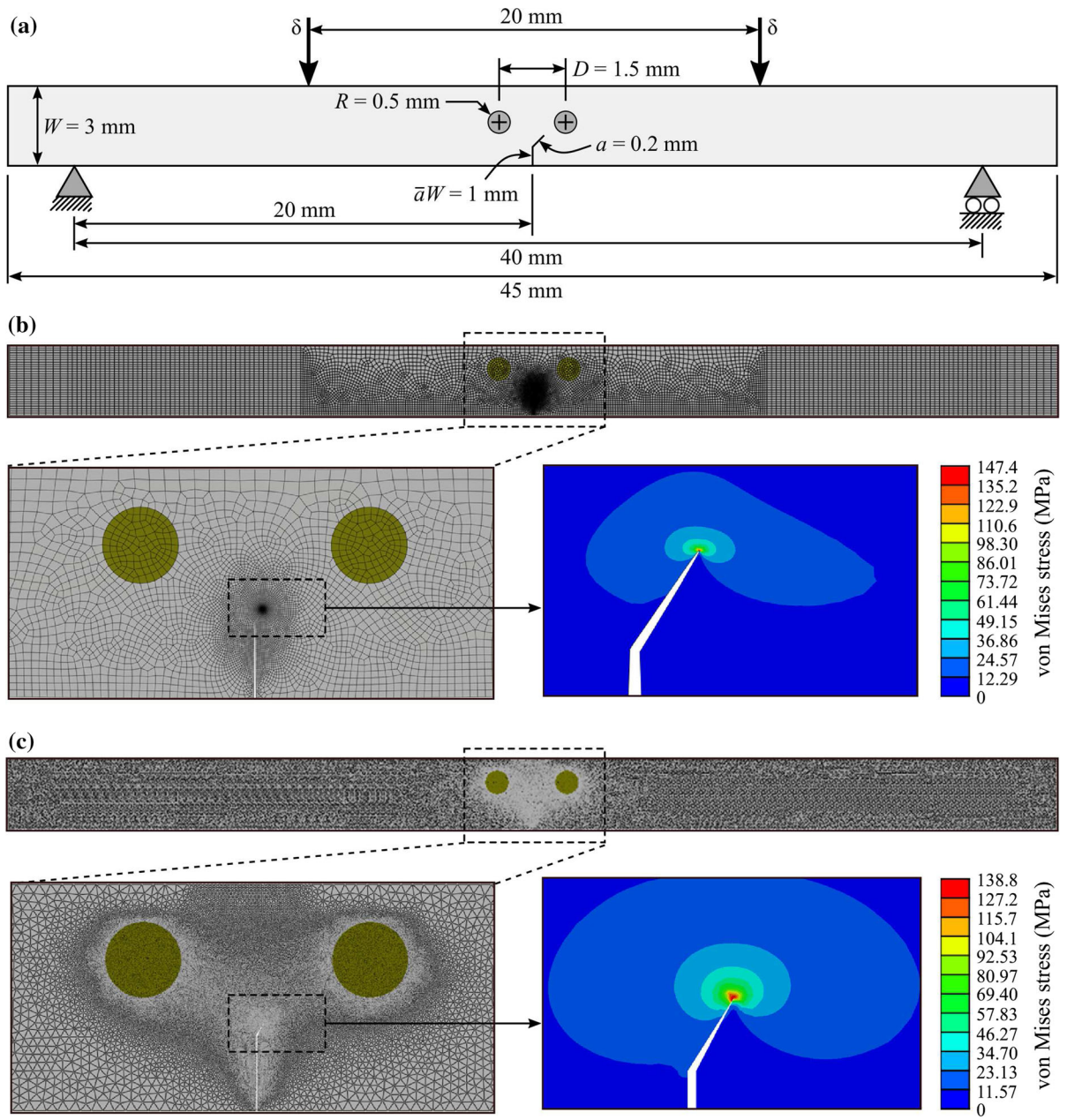

Fig. 2 A schematic of the specimen in **a** shows the geometry, loading and boundary conditions for the 4-point bending test, which includes the dimension of the inclusions and kinked crack. The mesh detail and von Mises stress contours are shown for the **b** LEFM model and **c** phase-field model

of the result from finite element analysis. The addition of the inclusions causes an increase in the stress intensity factors and J-integral relative to the homogeneous case. This is expected for the case of compliant inclusions considered here (cf. Table 1), which tend to increase the stress field near the crack tip. Furthermore, as shown in Fig. 3, increasing the size of the inclusion results in an increased J-integral. The reduced accuracy of the analytical model for large inclusion sizes is consistent with the underlying assumption of

Table 1 Material properties of the matrix and inclusion materials used in experiments and finite element analysis

Parameter	Symbol	Value
Matrix		
Young's modulus	E_{mat}	512 GPa
Poisson's ratio	ν_{mat}	0.16 (–)
Coefficient of thermal expansion from 300 to 1073 K	CTE_{mat}	6.6×10^{-6} K^{-1}
Critical energy release rate	$G_{c,\text{mat}}$	0.02674 N/mm
Inclusion		
Young's modulus	E_{inc}	2.55 GPa
Poisson's ratio	ν_{inc}	0.17 (–)
Coefficient of thermal expansion from 273 to 373 K	CTE_{inc}	4.3×10^{-6} K^{-1}
Critical energy release rate	$G_{c,\text{inc}}$	0.035 N/mm

The elastic properties of the matrix were measured via the impulse excitation technique while the remaining properties were obtained from the supplier (H. C. Starck). The properties of the inclusion were also obtained from the supplier (Goodfellow)

the inclusion radius being small compared to the crack length.

3 Fracture propagation

3.1 Incremental crack extension method

To predict the propagation of a crack, we propose an incremental crack extension method. First, an initial crack tip location is chosen. Then a small kink is added to the end of the crack. Using the fracture initiation model based on the J-integral of the kinked crack, the kink angle resulting in the maximum J-integral is found numerically. That is, find the kink angle, ω, that maximizes J in (5). This kink angle is taken to be the preferred propagation direction. Once the preferred propagation direction is determined, the new crack tip is found by adding a small crack increment of length, $\Delta a = 0.001$ mm, in the preferred direction. Then, the process is repeated to find the new preferred propagation direction from the current crack tip. Contour plots of the spatial variation of the maximum J-integral and its corresponding kink angle are show in Fig. 4a, b, respectively. The inclusion separation distance was $D = 1.5$ mm and the inclusion radii were $R = 0.3$ mm. The material properties used were the same as Table 1 (and taking $\nu = 0.16$). One can see in Fig. 4a that the maximum J-integral (of all kink directions) increases closer to the inclusions. In addition, the kink angle giving rise to the greatest J-integral tends to point towards the left inclusion when the crack is on the left half of the specimen and vice-versa on the right-half, as shown in Fig. 4b.

This is, of course, an approximation because the crack path behind the tip is not accounted for (each iteration assumes a straight crack up to the current crack tip location). However, this approach does provide a first approximation of the crack path as most of the material behind the crack tip becomes unloaded and thus does not significantly affect the stress at the crack tip.

3.2 Phase-field model

To gauge the accuracy of the crack extension method, we compare the estimated crack paths from the proposed approach with those predicted from a phase-field simulation and experiments. While the phase-field approach is common for predicting crack paths, the incremental crack extension method is a more computationally efficient alternative to obtain a first approximation of the crack paths through the composite. This is especially helpful as a first pass to sample the very large space of possible composite materials and geometric combinations.

The fundamental idea in brittle fracture is that a crack forms in order to minimize the internal energy (a combination of strain energy and crack surface energy), which dates back to the work of Griffith and Taylor (1921). Assuming linearized kinematics, the internal energy of a solid occupying a region Ω with a crack surface Γ is

$$U = \int_{\Omega/\Gamma} \psi(\boldsymbol{\varepsilon})\, \mathrm{d}V + \int_{\Gamma} G_c\, \mathrm{d}A, \tag{6}$$

where ψ is the strain energy density defined such that the stress is given by $\boldsymbol{\sigma} = \partial\psi/\partial\boldsymbol{\varepsilon}$ and $\boldsymbol{\varepsilon}$ is the small-strain tensor (since ceramic composites are being considered, the assumption of linearized kinematics is appropriate). The crack surface energy density is G_c. Note that the crack surface energy takes on different values, $G_{c,\text{inc}}$ and $G_{c,\text{mat}}$, depending on if the crack is in the inclusion or matrix, respectively. In the phase-field approach, the surface integral is transformed into a volume integral to simplify the numerical

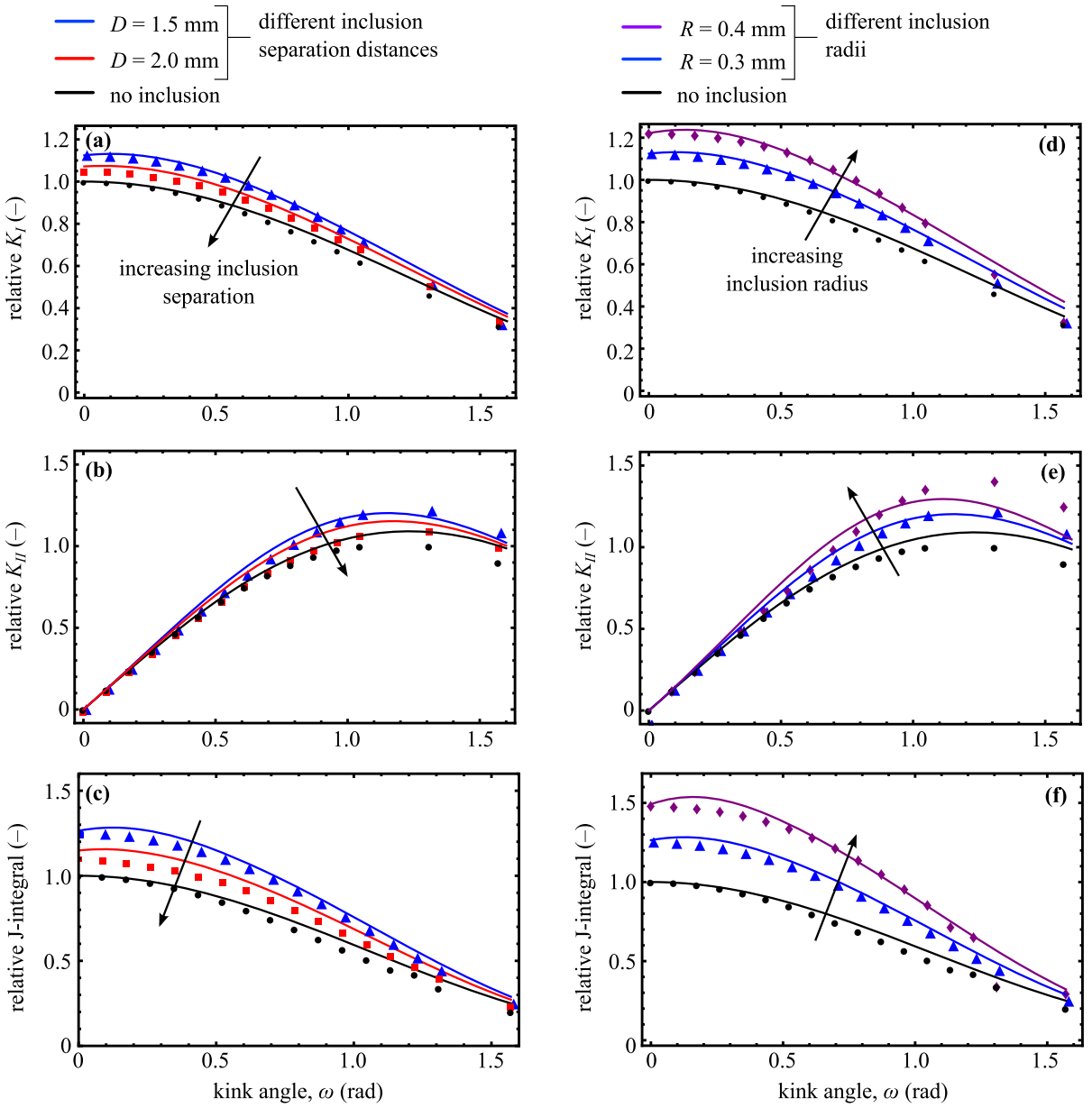

Fig. 3 Comparison between analytical model (lines) and linear elastic finite element simulation (dots). The left column shows the effect of different inclusion separation distances, D; **a**, **b**, and **c** compare the model and simulation values of the mode I and II stress intensity factors, and the J-integral versus kink angle, respectively. The right column shows the effect of different inclusion radii, R; similarly, **d**, **e**, and **f** compare the model and simulation values of the mode I and II stress intensity factors, and the J-integral versus kink angle, respectively

implementation of the model via a degradation function $\phi(\boldsymbol{x}) \in [0, 1]$ (Bourdin et al. 2008; Miehe et al. 2010). The internal energy is then,

$$U = \int_{\Omega} \left((1-\phi)^2 + k\right) \psi(\boldsymbol{\varepsilon})\, \mathrm{d}V + \int_{\Omega} \frac{G_c}{2} \left(\ell_0 \nabla\phi \cdot \nabla\phi + \frac{1}{\ell_0}\phi^2\right) \mathrm{d}V, \tag{7}$$

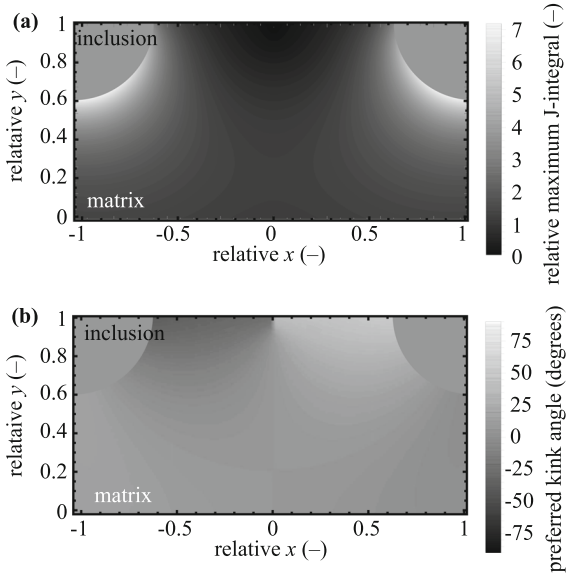

Fig. 4 Contour plots of the **a** J-integral and **b** kink angle in the preferred direction. The J-integral was normalized by its value for the straight kink at the origin. The coordinate axes are normalized by the inclusion separation distance, $D/2$

where now the degraded stress is $\boldsymbol{\sigma} = \partial\varphi/\partial\boldsymbol{\varepsilon}$, with $\varphi = ((1-\phi)^2+k)\psi(\boldsymbol{x}, \boldsymbol{\varepsilon})$ being the degraded strain energy density function. The material is completely fractured where $\phi = 1$ and is undamaged where $\phi = 0$. Also, we let ψ depend on the spatial position $\boldsymbol{x}$ since we will be considering composite materials with different elastic moduli. Hence, the strain energy function will vary with position. The parameter, $k = 10^{-5}$, is a small number for numerical conditioning. The crack width is characterized by ℓ_0. The potential energy term, Π, can then be obtained by subtracting the work done by external forces on the solid, $W = \int_\Omega \boldsymbol{b}\cdot\boldsymbol{u}\,\mathrm{d}V + \int_{\partial\Omega}\boldsymbol{t}\cdot\boldsymbol{u}\,\mathrm{d}A$, from the internal energy of the solid, U. That is, $\Pi = U - W$, where $\boldsymbol{b}$ is the body force, $\boldsymbol{t}$ is the surface traction, and $\boldsymbol{u}$ is the displacement field.

The results for the Euler–Lagrange (equilibrium) equations that minimize the potential energy are shown in Table 2. We implement this material model within the finite element method framework of Abaqus using subroutines including UMAT and UEL. Constant strain triangle elements were used with a single integration point (see Fig. 2c). The material parameters used in the phase-field model are the same as those used in the finite element simulation, which are shown in Table 1. However, in addition to Table 1, the intrinsic length scale parameter, ℓ_0, in the phase-field model was taken to be 1% of the inclusion diameter.

3.3 Specimen preparation for 4-point bending experiments

To fabricate composite specimens to use in validation experiments, a powder-based sintering approach was used (Hilmas and Watts 2006). The procedure is detailed in Fig. 5. Fabricating composites comprised of multi-phase constituents depends on their thermo-mechanical properties, geometry, size, and nature of the interface between them (Makarian et al. 2016). For the experiments, materials were selected that best mimicked the system analyzed in Fig. 1. In particular, materials with similar Poisson ratios and comparable coefficients of thermal expansion (to reduce residual stress and interface cracking from the sintering process) were selected. To this end, a zirconium diboride matrix and graphite inclusions were chosen (refer to Table 1 for material properties). A batch of powdered grade B zirconium diboride (93.86 wt.%) by H. C. Starck with phenolic resin (2.3 wt.%), boron carbide (0.98 wt.%), and traces of polyethylene glycol and polyvinyl butyral (PVB) were added as a binder and plasticizer, respectively, to the mix for the matrix. A batch of graphite (47.42 wt.%), methoxy polyethylene glycol MPEG (0.91 wt.%), heavy mineral oil (3.67 wt.%), polyether block amide PEBA-7 (24.83 wt.%), zirconium diboride (23.17 wt.%) and phenolic resin was prepared for the inclusion. These compositions are summarized in Table 3. The carbon and boron carbide additives to the ZrB_2 batch promote its densification (Neuman et al. 2017). These batches were ball milled in acetone for 24 h at ambient temperature and pressure using tungsten carbide milling media. The solution was then dried via rotary vacuum evaporation to obtain powder mixtures suitable for densification.

For the inclusion material, graphite powder was blended with the thermoplastic polymer and plasticizers (Table 3) using a torque rheometer at 130 °C and 30 RPM. This material was formed into a cylindrical feed-rod using a heated hydraulic press. This feed rod was then extruded into finer filaments with the desired diameters using a ram extruder. For the matrix, the powdered mixture batch (Table 3) was molded into billets of desired dimensions using a rectangular die and hydraulic press before drilling at selected inclusion

Table 2 The Euler–Lagrange equations of the potential energy used in the phase-field model

Symbolic	Index notation	Description
$\nabla \cdot \boldsymbol{\sigma} = \mathbf{0}$	$\sigma_{ij,j} = 0$	Stress equilibrium
$\boldsymbol{\sigma}\, \boldsymbol{n} = \boldsymbol{t}$	$\sigma_{ij,j}\, n_j = t_i$	Traction relation
$\frac{\partial \varphi}{\partial \phi} + \frac{G_c\, \phi}{\ell_0} + G_c\, \ell_0\, \nabla^2 \phi = 0$	$\frac{\partial \varphi}{\partial \phi} + \frac{G_c\, \phi}{\ell_0} + G_c\, \ell_0\, \phi_{,ii} = 0$	Degradation function PDE
$\nabla \phi \cdot \boldsymbol{n} = 0$	$\phi_{,i}\, n_i = 0$	Boundary condition of degradation function

Note that the summation convention is implied in the index notation form and commas denote differentiation with respect to the spatial coordinates

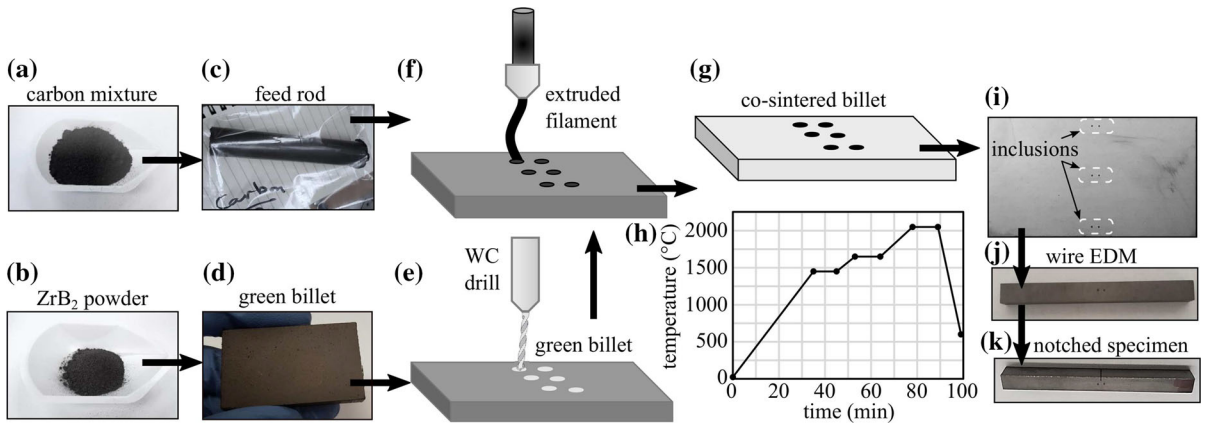

Fig. 5 Illustration of specimen fabrication process showing the **a** carbon mixture for inclusions, **b** ZrB_2 powder for matrix, **c** carbon feed rod, **d** ZrB_2 green billet, **e** periodic holes drilled into the green billet, **f** carbon feed rod extruded into filaments, **g** co-sintered ZrB_2-C billet, **h** sintering schedule, **i** ceramic composite with inclusions, and **j**, **k** the test specimens cut and notched

Table 3 Composition of the composite specimens

Material	Quantity (wt.%)
Matrix	
Zirconium diboride (grade B)	96.67
Phenolic resin	2.35
Boron carbide	0.98
Polyethylene glycol	Trace
Polyvinyl butyral (PVB)	Trace
Inclusion	
Graphite	47.42
Methoxy polyethylene glycol (MPEG)	0.91
Heavy mineral oil	3.67
Polyether block amide (PEBA-7)	24.83
Zirconium diboride	23.17

locations using fine 0.5 mm diameter, tungsten carbide drill bits. Then the graphite filaments were threaded through the matrix and the resulting sample was co-sintered in a graphite hot-press (Model HP20-3060; Thermal Technology Inc., Santa Rosa, CA) to form the precursor to the final specimen (typical overall billet dimensions were $40 \times 30 \times 5$ mm^3 with 500 μm diameter inclusions). The specimens were heated under vacuum (200 mTorr) with approximately 1 hour isothermal holds at both 1450 °C and 1650 °C. Following the 1650 °C hold, the atmosphere was changed to flowing argon and a pressure of 32 MPa was applied. The specimen was then ramped to the final densification temperature of 2050 °C. A ramp rate of 75 °C/min was maintained for the first two holds and then a ramp rate of 60 °C/min was applied until the densification temperature was attained. The ram travel was monitored upon reaching the final temperature to determine when the densification process ceased before cooling. The planar surfaces of the resulting sintered billets were ground using a Chevalier FSG-618 surface grinder with a 400 grit diamond grinding wheel with progressively finer diamond abrasives from National Diamond Lab. The

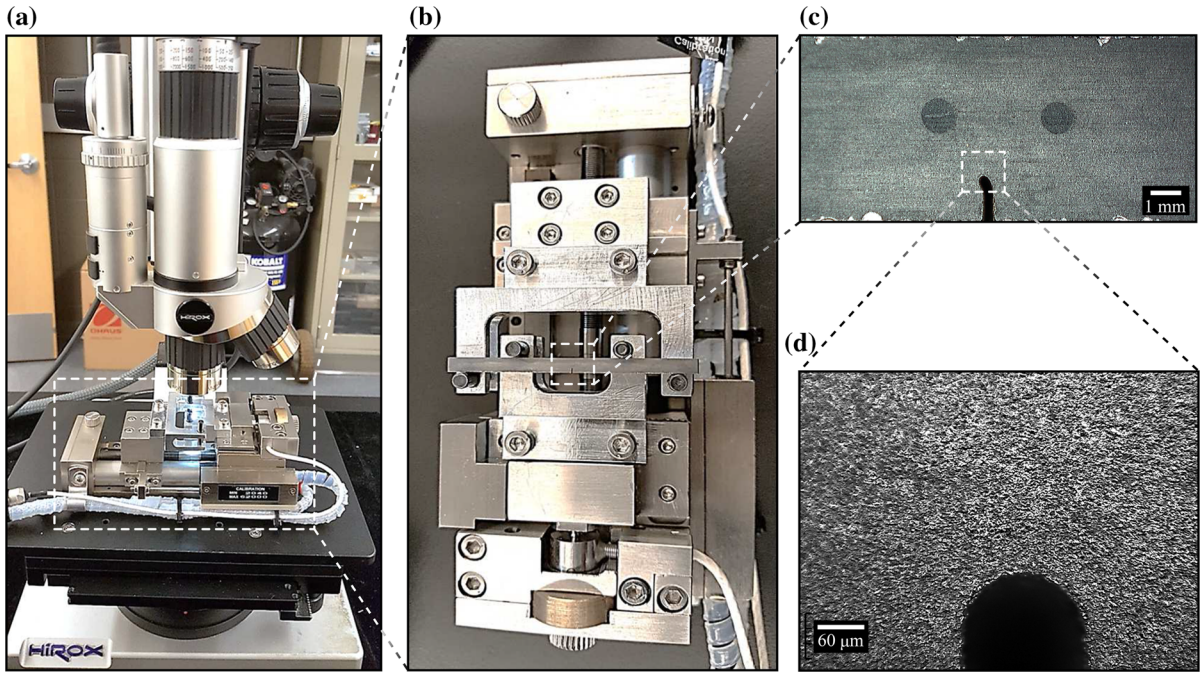

Fig. 6 Images of the **a** experimental set-up, **b** micro-tensile tester equipped with 4-point bending test fixture, **c** specimen with kinked notch and inclusions, and **d** the crack-tip

resulting surface finish facilitated the observation of the specimen under the microscope during experiments. The polished billets were then cut into the desired specimen size through wire electrical discharge machining (EDM).

A straight notch centered between the inclusions was introduced in one specimen and an off-set notch was introduced in the second specimen via wire electrical discharge machining. These specimens were subjected to a four-point-bend test using a 200 N lead-screw micro-tensile tester by Deben-GATAN and were observed under Hirox Digital KH-8700 optical microscope as illustrated in Fig. 6.

The bonding between the inclusion and matrix is of great importance when attempting to alter crack propagation using the inclusions. A key factor towards improving the bond strength is to use materials for the matrix and inclusion with comparable coefficients of thermal expansion since the main cause of debonding is residual stress arising during the sintering process (due to mismatched coefficients of thermal expansion), which cause cracks to form. Composites with second-phase inclusions are particularly susceptible to stress-induced micro cracking due to the localized stress fields formed during the co-sintering process (Green 1981). In addition, spontaneous interface failures are particularly prominent in materials with large elastic mismatch.

The inclusion size required to reduce interface fracture during sintering is a function of critical stress intensity factor, Poisson's ratio, and residual stress (Green 1981). Generally, smaller inclusions have a smaller interaction volume with the surrounding matrix and, as a result, exhibit less residual stress. This in turn reduces the likelihood of cracking. In addition, selecting materials with comparable coefficients of thermal expansion will mitigate interface fracture. Preliminary composite specimens containing zirconium diboride with graphite inclusions with diameters of approximately 500 µm resulted in no noticeable crack formation at the interfaces.

With the above manufacturing constraints, it would appear that the possible choices of materials and geometries are quite restricted. However, if certain material combinations are found to be desirable based on simulation results, but manufacturing such specimen results in interface debonding, there are other manufacturing routes that could be employed to reduce residual

stresses. For example, recent work (Els 2014; Hilmas et al. 2012) has focused on creating spiral shaped inclusions whose geometry reduces the residual stress. The spiral inclusion shape is formed by rolling layers of the inclusion and matrix material together, followed by co-extrusion into fibers to obtain the desired inclusion composition and geometry. Such spirals could be used in place of cylindrical inclusions. The spiral would practically behave as a cylindrical inclusion with its effective elastic modulus based on the relative volume fractions of materials forming the spiral. However, the introduction of such spiral inclusions is beyond the scope of this project.

Two types of specimens were produced with different crack offsets (relative to the central axis between the inclusions). For the specimens, the separation distance between the inclusions was the same, $D = 1.8$ mm. The diameter of the inclusions was 500 μm. For one type, the initial notch was half way between the inclusions while for the other, the initial notch was placed 0.5 mm to the right of the central axis. Both were loaded to failure. The fracture path is shown for each specimen in Fig. 7a. The load vs. load point displacement curve obtained from the experiments and phase field simulations for the aforementioned specimens with an off-set notch and a centered notch are illustrated in Fig. 7c. From the experiments, the maximum load before the ultimate failure of the specimen was 28% higher for the specimen with the off-set notch than the centered notch, 66 N and 52 N, respectively. This further illustrates the result that purely geometrical effects can be used to alter (and increase) the failure load (i.e. strength). Moreover, by examining the fracture paths between the two cases, the fracture surface area in the specimen with the off-set notch is higher than in the centered notch. Thus, the presence of inclusions near the initial crack results in increased crack surface area (and subsequently increased energy dissipation and toughness) by solely altering the geometry.

4 Discussion

4.1 Validation of proposed approach

To validate the proposed approach, the experimentally observed crack path was compared with the computed crack paths from the crack extension method and the phase-field model as shown in Fig. 7. Figure 7a shows the experimentally observed crack path for the two specimens with different initial notch positions. Figure 7b combines the crack paths obtained from the experiments (transcribed from microscope images), phase-field model, and crack extension method. The phase-field crack prediction was determined by plotting the line of maximum crack set parameter, ϕ. The trend of the fracture path predicted by the crack extension method follows the experimentally measured crack initially but deviates slightly as the crack approaches the inclusion, which is consistent with the various assumptions in the model. Also, the phase-field prediction follows both the experimentally measured crack and the crack extension method. While the phase-field result is slightly closer to the experimentally measured crack than the crack extension method, the phase-field method required significantly more time to compute. For comparison, the crack extension method required on the order of seconds to generate the path shown in Fig. 7, while the phase-field method required on the order of hours to simulate the corresponding path. While a detailed comparison of the run time between the two methods is beyond the scope of the paper, the order of magnitude difference in run time illustrates, qualitatively, the efficiency of the crack extension method over the phase-field approach, while maintaining accuracy.

With the accuracy of the analytical model established through LEFM finite element analysis, phase-field modeling, and an experimental case study, it was applied to investigate the influence of the inclusion properties and arrangement on the crack behavior in the matrix. In the following sections, the material characteristics, in particular the Young modulus mismatch, geometry, and the location of the inclusions with respect to the crack-tip are shown to affect the crack initiation and subsequently the propagation through the matrix material.

4.2 Relative crack length increase metric

In order to quantitatively compare the effectiveness of different composite designs on increasing the overall toughness of the material, the relative crack length increase metric was used, L/L_H, where L is the total length of the crack as it passes through a unit cell of inclusions and L_H is the length of a straight crack passing the same unit cell (if the material was replaced by a

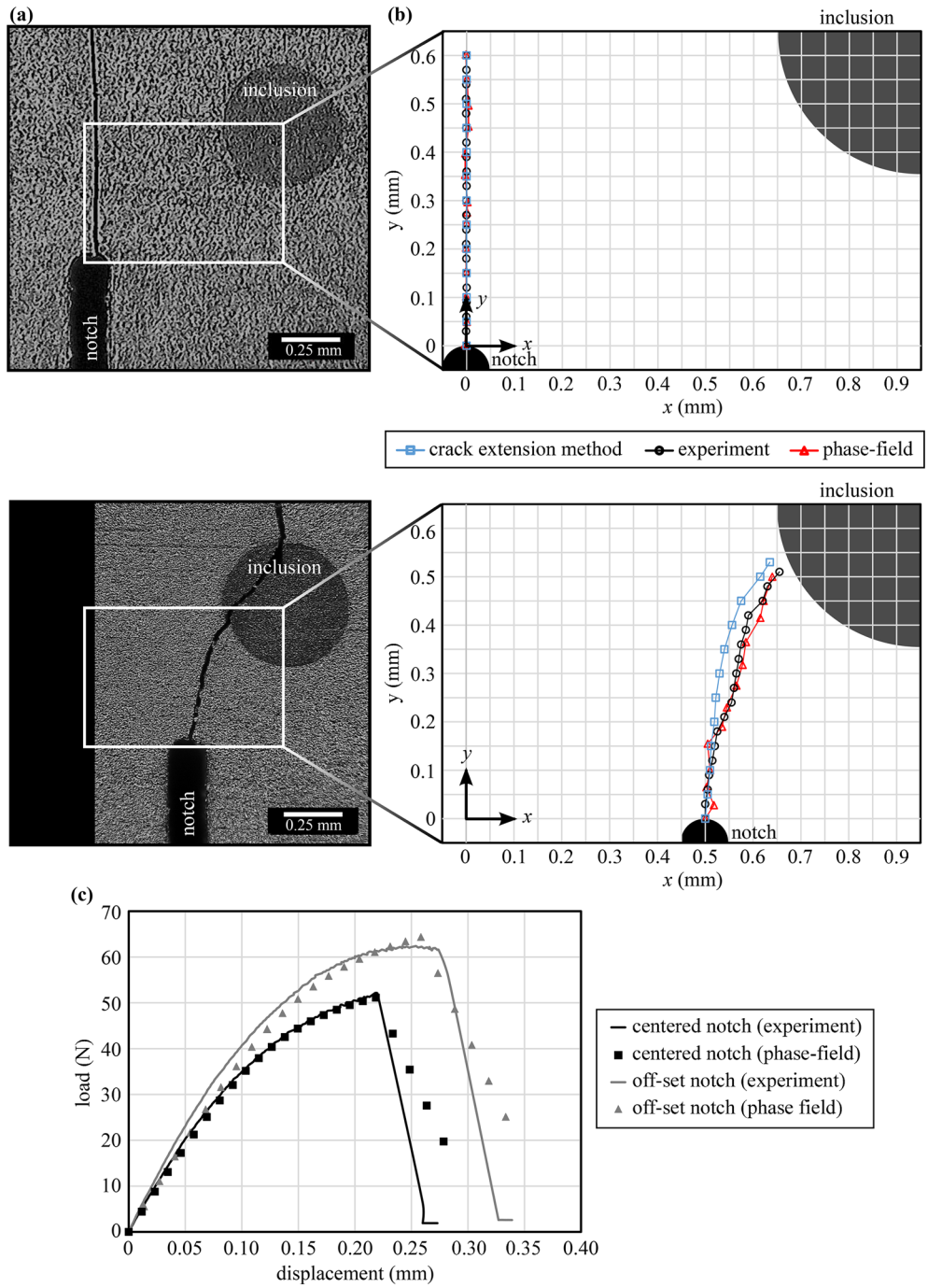

Fig. 7 **a** Experimental crack paths after complete fracture for varying notch locations. The size of the bottom image was not sufficiently large to completely visualize the denoted plotting area. Thus, the dark shaded region was added to the left side of the image. **b** Crack paths from the proposed method, phase field model, and experiment. **c** Load vs. load point displacement curve from the experiment and the phase field model illustrating variation in failure load and subsequently toughness between specimens with centered and off-set notch

homogeneous one). In linear elastic fracture mechanics, the energy dissipated due to crack propagation is transferred into the energy of the new surface area. In two dimensions, the size of the crack surface area is proportional to the length of the crack. In the following, we restrict our analysis to consider the case where the fracture propagates through the matrix (i.e. it does not intersect with inclusions). This is due to the corresponding assumption made in the stress intensity factor calculation. In other words, the following study of the effect of composite design on toughness focuses on the mechanism of crack deflection within the matrix. In this setting, the ratio of the energy dissipated in one unit cell between a homogeneous and composite specimen (quantifying the relative toughness), is equal to the relative crack length increase metric,

$$\frac{G_{c,\mathrm{mat}} A}{G_{c,\mathrm{mat}} A_H} = \frac{L}{L_H}, \tag{8}$$

where A and A_H are the surface areas of the crack in the composites compared to a homogeneous material. In the two dimensional analysis, a unit depth is assumed.

4.3 Influence of inclusion separation distance on fracture

An obvious factor to consider when designing a composite with an array of inclusions is to examine the effect of the spacing between the inclusions. In particular, it is important to understand the ability of the inclusions to affect the fracture process. To illustrate this effect, fracture paths from the phase-field simulation and the crack extension method are computed assuming different initial starting points between the center line, at $x = 0$, and the inclusion, at $x = D/2$, in increments of 0.1 mm as shown in Fig. 8a (for two different ratios of the inclusion separation to the radius, R/D); the crack extension method and phase-field model are compared again here in order to assess the accuracy of the analytical model as crack paths pass closer to the inclusions. As can be seen in the two plots of Fig. 8a, for larger crack offsets (resulting in a crack path that is also closer to the inclusion), the deviation of the crack extension method from the phase-field simulation increases, which is consistent with the assumptions in the model regarding the coupling between the inclusion and crack tip. Quantitatively, in the left plot of Fig. 8a,

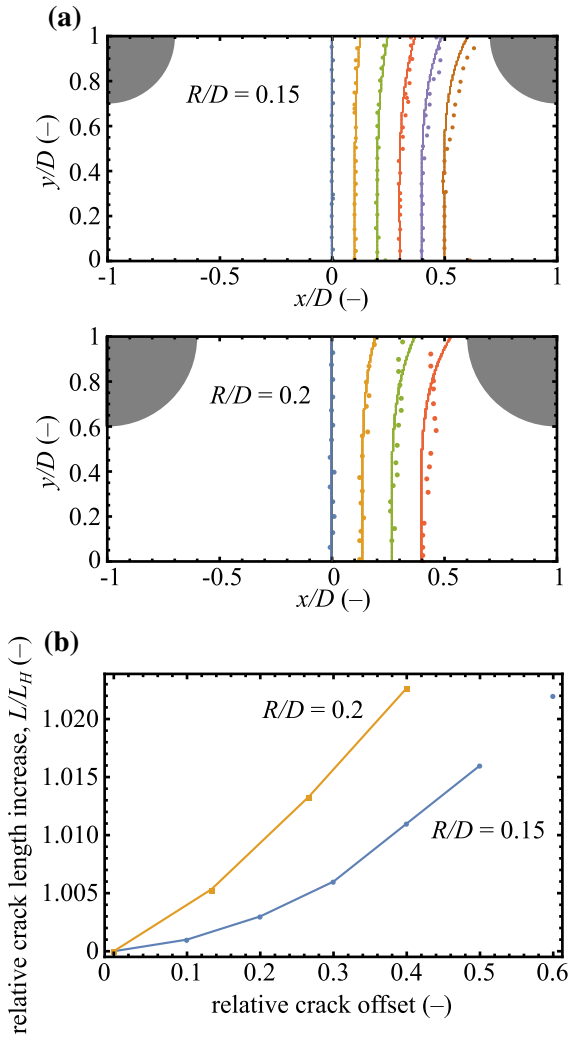

Fig. 8 Simulation of **a** crack propagation for different initial crack offset positions (the solid line denotes the crack extension method and the dots show the phase-field simulation) and **b** crack length increase versus inclusion separation and offset position predicted from the crack extension method. All distances are relative to the inclusion separation distance, D

with $R/D = 0.15$, the percent difference between the crack extension method and phase-field simulation (relative to the inclusion separation, D) for each crack path is 0.3, 2.5, 6.5, and 12.0%, for the cracks with initial offsets of $x = 0$, 0.1, 0.2, and 0.3 mm, respectively. Thus, the error of the extension method increases as the crack path passes closer to the inclusion. Qualitatively, however, the crack extension method is able to capture the same trend of the inclusions having a greater impact on the crack as it passes closer to the inclusion.

Again, it should be emphasized that the main advantage of the crack extension method is that it can be used as a first approximation to begin narrowing down the design space due to its computational efficiency. Simulating the entire design space with the phase-field method may not be feasible depending on the computational resources available.

It is intuitive that the smaller the separation distance between the inclusions is, the closer the fracture pathway is to the adjacent inclusion. Consequently, the closer the crack passes to the inclusion, the influence of the inclusion on the crack path is higher. This is illustrated in Fig. 8b, which plots the relative percent increase in crack length (relative to the straight crack) where the separation distance, D, between the inclusions was changed between 1.5 and 2 mm and their radius $R = 0.3$ mm was held fixed. In dimensionless terms, Fig. 8b shows the results for specimens with $R/D = 0.15$ and 0.2. It can be observed that the relative percent increase in the crack length, which correlates with the influence of the inclusion, is more significant for a given crack location offset for specimens with smaller inclusion separation distance for a fixed applied loading condition. An increase in crack length implies a larger crack surface area (and subsequently increased energy dissipation and toughness), thereby altering the fracture toughness of the specimen solely by varying the location of the inclusions within the matrix.

4.4 Effect of the inclusion pattern on the overall toughness

The crack extension method was used to study three composite designs, motivated by the results of Wei et al. (2019), in order to determine the one resulting in the greatest toughness enhancement. The three designs scenarios were (1) a cubic array of stiff inclusions rotated by an angle relative to the initial crack in order to guide the crack, (2) a body-centered cubic array of stiff inclusions to create a zig-zag pattern that increases crack length, and (3) a multi-phase cubic array of stiff and soft inclusions to also create a zig-zag pattern that increases crack length.

4.4.1 Crack guiding using a rotated cubic array

Altering the direction of crack propagation is useful for increasing the crack length (and therefore also the energy dissipated) as well as deflecting a crack away from a sensitive component in a material or structure. In this design, stiff inclusions are selected in order to contain the crack propagation within the matrix. A cubic array with $n = 16$ circular inclusions with variable radius R, and fixed spacing $D = 1.5$ mm, were simulated, such that $R/D \in \{0.13, 0.93\}$. This is accomplished by using the crack extension method based on the stress intensity factor in (4) where now the number of terms in the summation is increased due to the additional inclusions. To guide the crack, the cubic array was rotated by an angle γ relative to the initial direction of the notch crack. In this study, we sought to determine the R/D ratio that gave rise to the largest relative crack length increase L/L_H. The longest crack length corresponded to the case with the largest possible array orientation angle γ, while containing the crack within the matrix. The simulations were repeated for three different values of elastic mismatch ratio: $\alpha = 2$, 5, and 10 (defined in (12)). To change the elastic mismatch ratio, the Young modulus of the inclusion was varied while the Young modulus of the matrix was held fixed as the value in Table 1. The initial notch was assumed to be centered relative to the inclusion array (denoted by the origin in the Fig. 9).

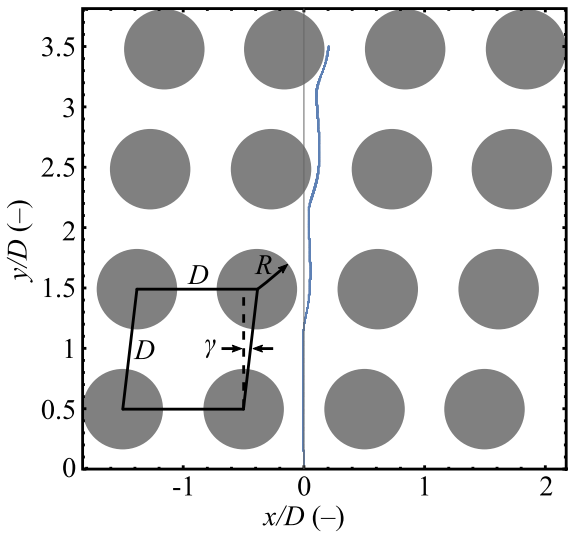

Fig. 9 Example cubic array of stiff inclusions ($\alpha = 10$ and $R/D = 0.3$), denoted by the shaded circles, oriented at an angle $\gamma = 7°$. The crack (blue line) is guided by the orientation of the inclusions

As an example, for the case of an elastic mismatch of $\alpha = 10$, and $R/D = 0.3$, the maximum angle of

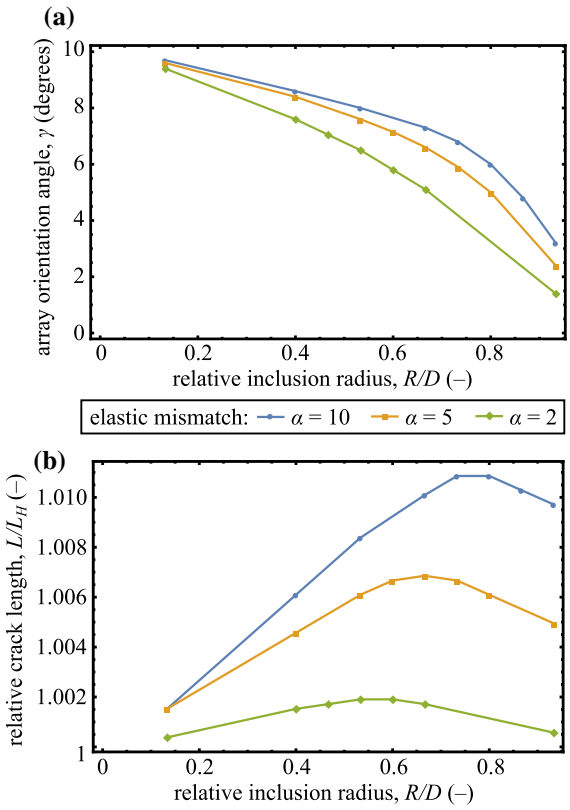

Fig. 10 **a** Plot of the maximum allowable orientation angle of the inclusions versus relative inclusion radius. **b** Plot of the corresponding relative crack length increase versus relative inclusion radius

the array orientation such that the crack remains in the matrix is shown in Fig. 9. If the orientation angle of the inclusions is further increased, the crack enters into the inclusions, which is not accounted for in the simplified model. If the orientation of the array is reduced, the crack is deflected less, resulting in a shorter crack length and lower toughness. In this particular design, the relative crack length increase was $L/L_H = 1.0078$.

In a similar manner the maximum angle of the inclusion orientation and the corresponding relative crack length increase were computed for different inclusion radii and elastic mismatch ratio, and are shown in Fig. 10a and b, respectively. One can see in Fig. 10a that as R/D increases, the maximum angle that the array can be rotated (while maintaining crack propagation within the matrix) decreases. This is because smaller inclusions can be shifted over a greater distance before intersecting the crack path (due to their smaller radii). The relative crack length increase versus inclusion radius in Fig. 10b interestingly shows a maximum. Generally, as R/D increases, it has a greater impact on crack deflection and thus the crack length increases. However, increasing R/D eventually has a negative impact on the crack deflection because the angle of the inclusion array must be reduced to prevent the crack from intersecting the inclusion. Thus, there is an important trade off between array orientation, γ, and R/D. Of the elastic mismatches considered, $\alpha = 2$, 5, and 10, the ratio of inclusion radius to spacing should be $R/D = 0.55$, 0.67, and 0.75, respectively, in order to maximize crack guiding for toughness enhancement.

4.4.2 Crack deflection using a body-centered cubic array

In the previous design scenario, the orientation of the array itself was used to deflect the crack and increase its length. In the proposed body-centered cubic array, the relative position of the inclusions is used as a mechanism to control the crack path as illustrated by the example in Fig. 11a. As with the previous example, the inclusion spacing is held fixed at $D = 1.5$ mm while the radius of the inclusions and elastic mismatch ratio were varied. The number of inclusions used was $n = 21$. The initial crack position was centered between the initial inclusion and the body-centered inclusion, i.e. at $x = D/4$. The result in Fig. 11a corresponds to $R/D = 0.24$ and $\alpha = 10$. For different combinations of inclusion radius and elastic mismatch ratio, the relative crack length increase L/L_H was computed (see Fig. 11b). One can see in Fig. 11b that as R/D increases, the relative crack length increases. However, the inclusion size cannot be increased arbitrarily large while containing the crack in the matrix. In this case, for $R/D > 0.24$, the crack will propagate in the inclusions (for each of the elastic mismatch ratios considered). For each radii, the crack length increase is higher for greater elastic mismatch. In summary, the maximum inclusion radius to spacing ratio was determined for the body-centered array and the corresponding crack length increase was computed.

Comparing the results in Fig. 11b with the previous results for the rotated cubic array in Fig. 10b, for similar combinations of inclusion radius and elastic mismatch ratio, the relative crack length increase is always higher for the body-centered cubic array than for the rotated cubic array. Thus, the local individual position of the inclusions has a greater effect on crack length (per unit

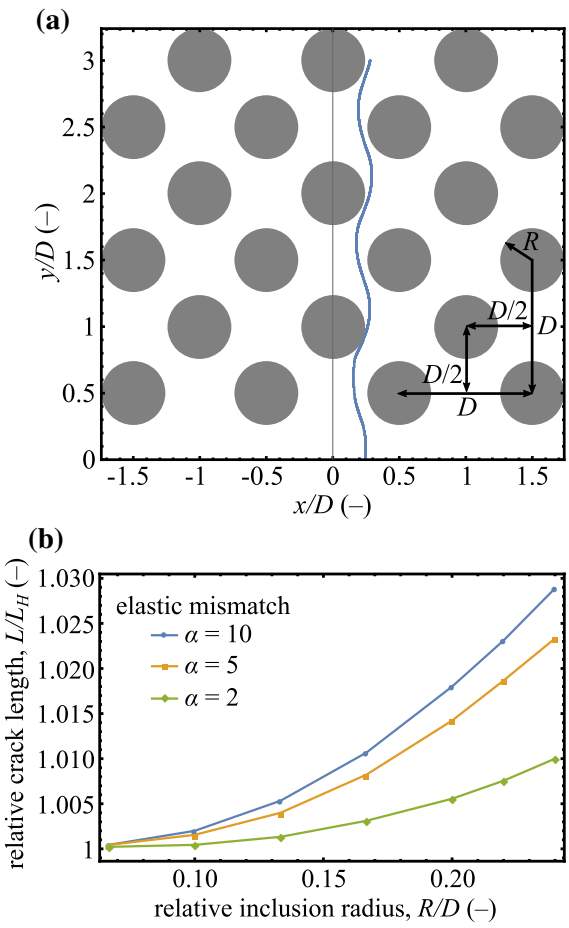

Fig. 11 **a** Body-centered cubic array of stiff inclusions used (shaded area) to increase the crack length (blue line). **b** Plot of the relative crack length increase versus relative inclusion radius

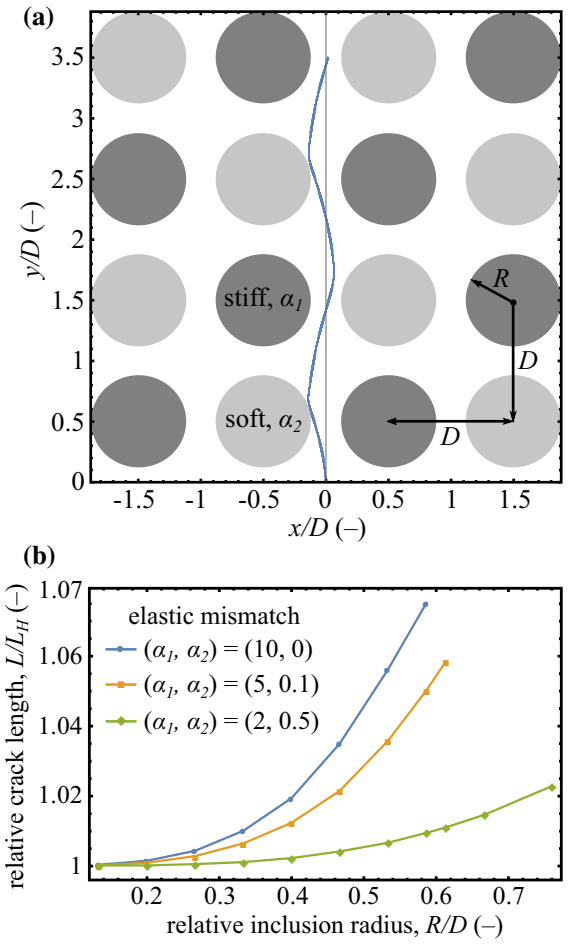

Fig. 12 **a** Inclusion arrangement in the multi-phase, cubic composite and resulting crack path. The dark and light shaded circles correspond to the stiff and soft inclusions, respectively. The crack path is denoted by the solid blue line. **b** Plot of relative crack length increase versus inclusion radius for different elastic mismatch ratios

cell) than the global deflection of the crack using the rotated cubic array. However, for crack guiding, the rotated cubic array can globally deflect and guide the crack, while changes in the local inclusion arrangement made possible in the body-centered cubic array only locally deflects the path while the global path remains fixed.

4.4.3 Crack deflection in a multi-phase array

As a final scenario, we consider the addition of a second (weak/soft) inclusion material to the previous consideration of only stiff inclusions. Motivated by the zig-zag behavior observed in Fig. 11a, the case of an alternating stiff and soft inclusion pattern was hypothesized to further increase the amplitude of the zig-zag behavior. For example, see Fig. 12a, which shows the arrangement of the stiff and soft inclusions in a cubic array. Generally, the crack is attracted to the soft inclusions and repelled by the stiff inclusions, resulting in the zig-zag behavior. With two different sets of inclusions, there are now two elastic mismatch ratios to consider corresponding to the strong/stiff inclusion and to the weak/soft inclusion,

$$\alpha_1 = \frac{E_{\text{stiff}}}{E_{\text{mat}}}, \quad \alpha_2 = \frac{E_{\text{soft}}}{E_{\text{mat}}}. \tag{9}$$

These two values of α are substituted into the expression for the coefficients in (11) for each inclusion that is added in the summation in (4). The three com-

binations of stiff and soft inclusions were the pairs: $(\alpha_1, \alpha_2) \in \{(10, 0), (5, 0.5), (2, 0.1)\}$. The crack propagation through composites with different inclusion radii and elastic mismatch ratios was simulated and the resulting relative crack length increase was determined and is shown in Fig. 12b. Generally, as R/D increases, the relative crack length increases due the increasing impact of larger inclusions on the crack path. However, for each combination of elastic mismatch, there exists a limit to how large the inclusions can be before the crack intersects the inclusions (corresponding to the largest value of R/D plotted on the axis). For greater elastic mismatch, the largest inclusion radii that can be used is reduced. However, for greater elastic mismatch (even with the limitation in maximum R/D), the relative crack length increase is higher for any R/D. In particular, for the multi-phase array, the relative crack length increase for the case of the greatest elastic mismatch was nearly $L/L_H = 1.07$, which is the largest observed (for the same elastic mismatch) of the previous designs, viz. the rotated cubic array and the body-centered cubic array. Therefore, the multi-phase composite design is the best design scheme for increasing crack length of the designs considered (albeit a more complex design due to the multiple inclusion materials); a larger design space of possible inclusion arrangements could result in a design that further improves the toughness, but this is beyond the scope of this work. Nonetheless, the efficient crack extension method would significantly reduce the computational resources required to sample and analyze the large design space.

5 Conclusion

New manufacturing methods have enabled a large design space of composites that can be manufactured. In order to search the large space for designs that enhance the overall toughness of ceramic composites, a computationally efficient crack extension method was developed. The proposed method can be used to predict the fracture behavior of composite designs on the order of seconds (compared to hours when using current approaches such as phase-field modeling), with minimal loss in accuracy. This was demonstrated by comparing the method to LEFM, a phase-field model, and experiments. In particular, the crack extension method was shown to capture the behavior of how nearby inclusions affect the propagation path (and final length) of the crack, which is the main mechanism of interest when designing the composites to increase toughness. Thus, the crack extension method is a useful tool for sampling the large design space of composite arrangements in an efficient manner that lays the groundwork for future optimization studies in order to find the configurations with the largest toughness.

The ability of the crack extension method to analyze different composite arrangements was demonstrated by studying a reduced design space of three different composite arrangements: (1) a rotated cubic array of stiff inclusions used to guide the crack path, (2) a body-centered cubic array of stiff inclusions that resulted in a zig-zag crack pattern that increases crack length, and (3) a cubic array of stiff and soft inclusions that further enhanced the zig-zag behavior. For each design, the toughness was assessed via the relative crack length increase. In design (1), for elastic mismatch ratios of $\alpha = 2$, 5, and 10, the arrangement should be chosen such that $R/D = 0.55$, 0.67, and 0.75, respectively, in order to achieve the greatest toughness enhancement for matrix fracture. For design (2), likewise an arrangement with $R/D = 0.24$ results in the greatest toughening (and is not sensitive to the elastic mismatch ratio). In (3), the inclusion arrangement with greatest matrix fracture toughness depends on R/D; for the largest elastic mismatch, $R/D = 0.6$ is the best design, while for the smallest elastic mismatch, $R/D = 0.8$ is the best design. Overall, the multi-phase composite demonstrated the greatest toughening for similar elastic mismatch compared to the other designs.

These results demonstrate the possibility of controlling crack growth using ordered inclusion arrays, which has been enabled by advanced manufacturing approaches. Furthermore, the computationally efficient crack extension method will aid in uncovering optimal designs of the composites for increasing toughness. Future efforts can utilize this fast-running method to carry out optimization studies where the position of each inclusion is considered as a variable to optimize over in order to span the entire design space.

Acknowledgements The authors acknowledge support from the NSF CMMI Award number 1930881. The authors also thank the Center of Infrastructure Engineering Studies and the Intelligent System Center at the Missouri University of Science and Technology for support.

Appendix A: Approximate stress intensity factor of a kinked crack in a 4-point bending test

The parameters c and d, used in (2) are functions of the kink angle, ω, with an infinitesimal kink length. This approximation is asymptotically accurate for small kink angles (in a homogeneous material) and is given by:

$$\begin{aligned} c &= \frac{1}{2}\left(\exp\left(-j\frac{\omega}{2}\right)+\exp\left(-j\frac{3\omega}{2}\right)\right), \\ d &= \frac{1}{4}\left(\exp\left(-j\frac{\omega}{2}\right)-\exp\left(j\frac{3\omega}{2}\right)\right), \end{aligned} \tag{10}$$

where $j = \sqrt{-1}$ (Cotterell 1965; He and Hutchinson 1989; Williams 1956).

Appendix B: Influence of a nearby inclusion on a straight crack

The perturbation in stress intensity factor in mode I and II fracture due to the difference in material properties of the inclusions and the matrix is dictated by the following coefficients appearing in (3):

$$\begin{aligned} C_1 &= \frac{(1-\alpha)(1-2\nu)}{1+\alpha-2\nu}, \\ C_2 &= \frac{3(1-\alpha)}{2(1+3\alpha-4\nu\alpha)}, \\ C_3 &= \frac{(1-\alpha)(11+19\alpha+32\nu^2\alpha-22\nu-40\nu\alpha)}{16(1+\alpha-2\nu)(1+3\alpha-4\nu\alpha)}, \\ C_4 &= \frac{-(1-\alpha)(1-2\nu)}{4(1+\alpha-2\nu)}, \\ C_5 &= \frac{9(1-\alpha)}{16(1+3\alpha-4\nu\alpha)}, \end{aligned} \tag{11}$$

where ν is Poisson's ratio (assumed to be same for the inclusions and the matrix) and

$$\alpha = \frac{E_{\text{inc}}}{E_{\text{mat}}} \tag{12}$$

is the ratio of the Young modulus of the inclusion, E_{inc}, to the Young modulus of the matrix, E_{mat}. Note that in most cases, the Poisson ratio of the composite materials will not be identical. Hence, the results predicted from this model will be most accurate when the Poisson ratios of the constituents are nearly the same value. Despite this assumption, the model is still able to accurately capture experimental results.

References

Anderson T (2005) Fracture mechanics: fundamentals and applications, 3rd edn. Taylor & Francis, London

Bourdin B, Francfort GA, Marigo JJ (2008) The variational approach to fracture. J Elast 91:5–148

Cotterell B (1965) On brittle fracture paths. Int J Fract Mech 1:96–103

Danzer R (1992) A general strength distribution function for brittle materials. J Eur Ceram Soc 10:461–472

D'Angio' A, Zou J, Binner J, Ma HB, Hilmas G, Fahrenholtz W (2018) Mechanical properties and grain orientation evolution of zirconium diboride–zirconium carbide ceramics. J Eur Ceram Soc 38:391–402

Els AL (2014) Development and characterization of spiral additions in a ceramic matrix. Master's thesis. Missouri University of Science and Technology

Eshelby JD (1975) The elastic energy-momentum tensor. J Elast 5:321–335

Evans AG, Wiederhorn SM (1984) Proof testing of ceramic materials—an analytical basis for failure prediction. Int J Fract 26:355–368

Faber K, Evans A (1983a) Crack deflection processes I. Theory. Acta Metall 31:565–576

Faber K, Evans A (1983b) Crack deflection processes II. Experiment. Acta Metall 31:577–584

Fett T, Diegele E, Rizzi G (1996) Calculation of stress fields near inclusions by use of the fracture mechanics weight function. Eng Fract Mech 53:17–22

Gao H, Ji B, Jäger IL, Arzt E, Fratzl P (2003) Materials become insensitive to flaws at nanoscale: lessons from nature. Proc Natl Acad Sci 100:5597–5600

Green DJ (1981) Stress-induced microcracking at second-phase inclusions. J Am Ceram Soc 64:138–141

Griffith AA, Taylor GI (1921) VI. The phenomena of rupture and flow in solids. Philos Trans R Soc Lond 221:163–198

He MY, Hutchinson JW (1989) Kinking of a crack out of an interface. J Appl Mech 56:270–278

Helsing J (1999) Stress intensity factors for a crack in front of an inclusion. Eng Fract Mech 64:245–253

Hilmas G, Watts J (2006) Tailoring the properties of ceramic-based composites using co-extrusion processing. In: 11th international ceramics congress, Trans Tech Publications Ltd. pp 1385–1393

Hilmas GH, Fahrenholtz W, Watts J (2012) Method for toughening via the production of spiral architectures through powder loaded polymeric extrusion and toughened materials formed thereby. U.S. Patent US8192853B2

Hoy CV, Barda A, Griffith M, Halloran JW (1998) Microfabrication of ceramics by co-extrusion. J Am Ceram Soc 81:152–158

Lambropoulos J (1986) Shear, shape and orientation effects in transformation toughening. Int J Solids Struct 22:1083–1106

Li Z, Chen Q (2002) Crack-inclusion interaction for mode I crack analyzed by Eshelby equivalent inclusion method. Int J Fract 118:29–40

Lipetzky P, Knesl Z (1995) Crack-particle interaction in a two-phase composite Part II: crack deflection. Int J Fract 73:81–92

Makarian K, Santhanam S, Wing ZN (2016) Coefficient of thermal expansion of particulate composites with ceramic inclusions. Ceram Int 42:17659–17665

Miehe C, Welschinger F, Hofacker M (2010) Thermodynamically consistent phase-field models of fracture: variational principles and multi-field FE implementations. Int J Numer Methods Eng 83:1273–1311

Miller R, Ortiz M, Phillips R, Shenoy V, Tadmor E (1998) Quasicontinuum models of fracture and plasticity. Eng Fract Mech 61:427–444

Neuman EW, Hilmas GE, Fahrenholtz WG (2017) Processing, microstructure, and mechanical properties of zirconium diboride–boron carbide ceramics. Ceram Int 43:6942–6948

Ritchie RO, Buehler MJ, Hansma P (2009) Plasticity and toughness in bone. Phys Today 62:41

Sih GC, Hilton PD, Wei RP (1970) Exploratory development o fracture mechanics of composite systems. Technical Report

Stam G, van der Giessen E, Meijers P (1994) Effect of transformation-induced shear strains on crack growth in zirconia-containing ceramics. Int J Solids Struct 31:1923–1948

Twickler R, Twickler M, Dahl W (1986) Two- and three-dimensional elastic-plastic stress analysis for a double edge notched tension specimen. Eng Fract Mech 24:553–565

Wang C, Libardi W, Baldo J (1998) Analysis of crack extension paths and toughening in a two phase brittle particulate composite by the boundary element method. Int J Fract 94:177–188

Wei C, Wu C, Wojnar C (2019) Effect of patterned inclusions on the fracture behavior of ceramic composites. Compos Part B Eng 172:564–592

Williams ML (1956) On the stress distribution at the base of a stationary crack. J Appl Mech 24:109–114

Yang L, Chen Q, Li Z (2004) Crack-inclusion interaction for mode II crack analyzed by Eshelby equivalent inclusion method. Eng Fract Mech 71:1421–1433